Phase field study of precipitate rafting under a uniaxial stress

M P Gururajan and T A Abinandanan

Department of Materials Engineering, Indian Institute of Science, Bangalore 560 012 INDIA

Abstract

We examine rafting of two-phase microstructures under a uniaxial applied stress, a process in which a mismatch in elastic moduli (elastic inhomogeneity) plays a central role. For this purpose, we have used a phase field model of an elastically inhomogeneous alloy; elastic stress and strain fields are calculated using a method adapted from the homogenization literature. We have characterized the efficiency of the resulting iterative algorithm based on Fourier transforms. Our simulations of rafting in two-dimensional systems show that rafting (unidirectionally elongated microstructures) is promoted when the precipitate phase is softer than the matrix and when the applied stress has the same sign as the eigenstrain. They also show that migration (for both hard and soft precipitates) and coalescence (for soft precipitates) have significant contributions to rafting.

Key words: phase field modelling, microstructure, homogenisation, rafting, elastic stress effects

1 Introduction

Elastic stresses arise during solid state phase transformations due to a lattice parameter mismatch between the participating phases. In addition, there may also be externally applied stresses. These stresses have a marked influence on the evolution of microstructures [1–4]. While some of these stress effects may be explained or rationalised by assuming that the phases have the same elastic moduli, other effects arise primarily due to a mismatch in elastic moduli (elastic inhomogeneity) of the phases. Examples of the latter include rafting in Ni-base superalloys [5], phase inversion [6], and instabilities in thin solid films [7]. This paper is on rafting; preliminary results for phase inversion and thin film instabilities were presented in [8].

The preferential coarsening of (dilatationally) misfitting precipitates in a direction parallel (P-type) or perpendicular (N-type) to an applied stress is known as rafting [5,9]: see [10] and [11] for reviews. There have been a number of attempts in the literature to determine the type of rafting due to elastic stresses [12–24]. Some of them – energy based approaches – examine the elastic energy of isolated precipitates under stress [12,13,15] to deduce energetically favourable particle shapes and orientations. Thermodynamic approaches, on the other hand, examine the instantaneous chemical potential contours around a single misfitting inhomogeneity [14,16] under stress. (These thermodynamic and energy-based studies are critically reviewed by Chang and Allen [10]. The kinetic studies of rafting are based on atomistic [21–24] or continuum models [17–20].

Thermodynamic studies (such as that of Schmidt and Gross [16]) indicate that the type of rafting is determined by the sign of misfit strain ε^T, sign of applied stress σ^A, and inhomogeneity δ, defined as the ratio of the shear modulus of the precipitate phase (G^p) to that of the matrix phase (G^m). We discuss these results in greater detail in Section 5.1.

Several recent studies have focussed on the effect of a plastic prestrain on rafting [9,25–28]. In particular, some of these studies argue that such a plastic prestrain is essential for rafting. On the other hand, there is at least one experimental study [29], the results of which are not able to choose between linear elastic and plastic theories; and, Nabarro [12] has argued that there is significant experimental evidence for rafting due to elastic stresses alone.

Our main aim in this paper, is to show that rafting occurs even under the assumptions of linear elastic constitutive laws, and that the thermodynamic models do predict the type of rafting correctly. We do go beyond this narrow objective, however, by studying multiparticle simulations to study the contributions of interparticle interactions (particle coalescence and migration) to rafting.

By definition, rafting in systems with dilatational misfit (or, eigenstrain) is possible only in systems with a mismatch in elastic moduli. Since elastic stresses in such inhomogeneous systems are harder to compute, there has been only limited progress in large scale simulations of rafting. In a system with a spatially periodic microstructure (used for modelling an effectively infinite system) under a constant traction at the boundary, one needs to compute both the periodic strain ε^* and a homogeneous strain $\mathbf{E}$ self-consistently. Such a self-consistent computational technique is available in the literature on homogenization since 1995 [30] (see also [31,32]). However, these techniques do not take into account an eigenstrain field (due to a lattice parameter mismatch between the two phases). Since stresses in our model arise from both an eigenstrain field and an applied stress, we have adapted the algorithm presented in

Ref. [31]. We present an outline of this algorithm in Section 3

Our phase field model with a Fourier spectral implementation is similar to that used in Refs. [33,19], who studied systems under a prescribed homogeneous strain $\mathbf{E}$. We, on the other hand, have studied rafting in systems under a prescribed applied stress (for which the homogeneous strain has to be calculated self-consistently).

We first present, in Section 2, the diffuse interface model based on the Cahn-Hilliard equation for microstructural evolution in elastically inhomogeneous systems. We then outline, in Section 3, the iterative solution technique for solving the equation of mechanical equilibrium under a prescribed displacement (constant applied strain) and prescribed traction (constant applied stress) at the boundary; the details can be found in [34]. In Section 4, we provide a few benchmarking results to demonstrate our method's accuracy and efficiency. In Section 5 we present our results on rafting in multiparticle systems. We end the paper with a discussion and a brief summary.

2 The Cahn-Hilliard model with elastic energy

We consider a binary phase separating A-B alloy system exhibiting a miscibility gap. At a low temperature, an alloy of composition c'_0 that finds itself inside the miscibility gap will consist of two phases m and p with compositions c'_m and c'_p, respectively, at equilibrium.

We rescale the composition variable c' to yield the scaled composition c:

$$c = \frac{c' - c'_m}{c'_p - c'_m}. \tag{1}$$

With this definition, the composition c of a two-phase alloy is the same as the equilibrium volume fraction of the p-phase; in particular c takes a value of zero and unity in the matrix and precipitate phases, respectively. Further, all the variables are rendered non-dimensional using a characteristic length L', energy E', and time T', a suitable choice for which is deferred to section 3.3. All the equations in our formulation are presented in terms of non-dimensional and scaled variables.

Let the composition at any point $\mathbf{r}$ at time t be denoted by $c(\mathbf{r}, t)$. Let the microstructure of the system be completely described by the composition field. Consider a domain Ω bounded by $\partial\Omega$ of such a system; we assume the composition field to be periodic on Ω. Given an initial microstructure (i.e., composition

profile), say c(**r**,0), its future evolution can be studied by solving the following version of the Cahn-Hilliard equation [35]:

$$\frac{\partial c}{\partial t} = \nabla \cdot M \nabla (\mu^{ch} + \mu^{el}), \tag{2}$$

where c is the (scaled) composition, M is the mobility, and t is time. μ^{ch} and μ^{el} are the chemical and elastic contributions, respectively to the chemical potential, defined as the variational derivatives of chemical (F^{ch}) and elastic (F^{el}) free energies, respectively, with respect to the local composition:

$$\mu^{ch} = \frac{\delta \left[\frac{F^{ch}}{N_V}\right]}{\delta c}, \tag{3}$$

and,

$$\mu^{el} = \frac{\delta \left[\frac{F^{el}}{N_V}\right]}{\delta c}. \tag{4}$$

The chemical free energy F^{ch} is given by the following expression:

$$F^{ch} = N_V \int_{\Omega} [f_0(c) + \kappa (\nabla c)^2] d\Omega, \tag{5}$$

where, κ is the gradient energy coefficient, and $f_0(c)$ is the bulk free energy density is assumed to be given by the following 'double well' potential:

$$f_0(c) = A_b c^2 (1-c)^2, \tag{6}$$

where A_b is a positive constant which sets the energy barrier between the two equilibrium phases m and p; thus,

$$\mu^{ch} = h(c) - 2\kappa \nabla^2 c, \tag{7}$$

with, $h(c) = (\partial f_0 / \partial c)$.

In this paper, we assume the mobility M in Eq. 2 and the gradient energy coefficient κ in Eq. 5 to be (scalar) constants: thus, the interfacial energies and the diffusivities to be isotropic.

The elastic contribution to the total free energy is given by [36]:

$$F^{el} = \frac{1}{2} \int_{\Omega} \sigma_{ij}^{el} \varepsilon_{ij}^{el} d\Omega \tag{8}$$

where, σ_{ij}^{el} is the elastic stress, and ε_{ij}^{el} is the elastic strain, given by:

$$\varepsilon_{ij}^{el} = \varepsilon_{ij} - \varepsilon_{ij}^{0}. \tag{9}$$

ε^0 is the position dependent eigenstrain field, and, ε_{ij} is the (compatible) total strain, given by

$$\varepsilon_{ij} = \frac{1}{2}\left\{\frac{\partial u_i}{\partial r_j} + \frac{\partial u_j}{\partial r_i}\right\}. \tag{10}$$

$\mathbf{u}$ is the the displacement field. Assuming both the m and p phases to obey Hooke's law (i.e., the phases are linear elastic), we have

$$\sigma_{kl}^{el} = C_{ijkl}\varepsilon_{ij}^{el}, \tag{11}$$

where C_{ijkl} is the composition dependent (and hence, position dependent) elastic modulus tensor.

The eigenstrain is assumed to be dilatational and an explicit function of composition:

$$\varepsilon_{ij}^{0}(c) = \beta(c)\varepsilon^{T}\delta_{ij}, \tag{12}$$

where, ε^T is a constant that determines the strength of the eigenstrain, δ_{ij} is the Kronecker delta, and $\beta(c)$ is a scalar function of composition.

The elastic modulus tensor is also an explicit function of composition. It is convenient to describe C_{ijkl} using the following expression:

$$C_{ijkl}(c) = C_{ijkl}^{\text{eff}} + \alpha(c)\Delta C_{ijkl}, \tag{13}$$

where $\alpha(c)$ is a scalar function of composition, and

$$\Delta C_{ijkl} = C_{ijkl}^{p} - C_{ijkl}^{m}, \tag{14}$$

and C_{ijkl}^{p} and C_{ijkl}^{m} are the elastic moduli tensor of the p and m phases respectively, and C_{ijkl}^{eff} is an "effective" modulus.

In addition, the entire macroscopic system could be subjected to a homogeneous stress state σ^A, i.e., the domain Ω behaves as if it is a single homogeneous block in spite of the inhomogeneities at the microscopic scale. Note that σ^A should be such that the applied traction on the boundaries of the domain Ω is

anti-periodic; i.e., $\sigma \cdot \mathbf{n}$, is opposite on opposite sides of $\partial\Omega$ with $\mathbf{n}$ being the unit normal to the boundary [31,30].

To obtain the elastic energy, and hence the elastic chemical potential, we have to solve the equation of mechanical equilibrium,

$$\frac{\partial \sigma_{ij}^{el}}{\partial r_j} = 0 \quad \text{in } \Omega. \tag{15}$$

The Fast Fourier Transform (FFT) based iterative method to solve the above set of partial differential equations is described below.

3 Solution to the equation of mechanical equilibrium

The elastic moduli and the eigenstrains are periodic on Ω (since they depend on composition field which is periodic on Ω); therefore, the solution to the equilibrium equation (Eq. 15), should be such that it gives rise to a strain field $\varepsilon(\mathbf{r})$ that is periodic on Ω (up to an additive constant). The displacement field $\mathbf{u}(\mathbf{r})$ which gives rise to such periodic strain fields can always be written as follows [30]:

$$\mathbf{u} = \mathbf{E} \cdot \mathbf{r} + \mathbf{u}^{\star}, \tag{16}$$

where, $\mathbf{u}^{\star}$ is a displacement field that is periodic on Ω and $\mathbf{E}$ is a constant, homogeneous strain tensor (assumed to be symmetric without loss of generality, since the antisymmetric part corresponds to a rigid rotation of the cell). It can be shown [30] that $\mathbf{E}$ denotes the mean strain tensor of the cell:

$$\langle \{\varepsilon_{ij}\} \rangle = E_{ij}, \tag{17}$$

with the following definition for the mean $\langle \{\cdot\} \rangle$ of a quantity $\{\cdot\}$:

$$\langle \{\cdot\} \rangle = \frac{1}{V} \int_{\Omega} \{\cdot\} d\Omega, \tag{18}$$

where V is the volume of the representative domain Ω.

If we denote the periodic strain by $\varepsilon^{\star}$, the strain that we derive from the displacement equation 16 becomes,

$$\varepsilon_{ij} = E_{ij} + \varepsilon_{ij}^{\star}, \tag{19}$$

where,

$$\varepsilon^{\star}_{ij} = \frac{1}{2}\left\{\frac{\partial u^{\star}_i}{\partial r_j} + \frac{\partial u^{\star}_j}{\partial r_i}\right\}. \tag{20}$$

Analogous to the expression 17 for the homogeneous strain, we can define the mean stress on the domain Ω as follows:

$$\langle\{\sigma^{el}_{ij}\}\rangle = \frac{1}{V}\int\limits_{\Omega} \sigma^{el}_{ij} d\Omega. \tag{21}$$

The mean stress thus calculated should equal the applied stress σ^A [30,31,37]. [As a brief aside, we note that while References [30] and [31] used the homogenisation assumption, Jin et al [37] used a variational approach to arrive at the above conclusion, viz., that the mean stress should equal the applied stress.] Substituting for σ^{el}_{ij} from Eq. 11, we obtain

$$\sigma^A_{ij} = \frac{1}{V}\int\limits_{\Omega} C_{ijkl}(E_{kl} + \varepsilon^{\star}_{kl} - \varepsilon^0_{kl}) d\Omega. \tag{22}$$

Further, using the definition in Eq. 18, we can define the following mean quantities:

$$S_{ijkl} = (\langle\{C_{ijkl}\}\rangle)^{-1},\ \langle\{\sigma^{\star}_{ij}\}\rangle = \langle\{C_{ijkl}\varepsilon^{\star}_{kl}\}\rangle,\ \text{and}\ \langle\{\sigma^0_{ij}\}\rangle = \langle\{C_{ijkl}\varepsilon^0_{kl}\}\rangle. \tag{23}$$

Using Eq(s). 22 and 23, we obtain

$$E_{ij} = S_{ijkl}\ \left[\sigma^A_{kl} + \langle\{\sigma^0_{kl}\}\rangle - \langle\{\sigma^{\star}_{kl}\}\rangle\right]. \tag{24}$$

We may restate the elasticity problem as follows: Given a periodic composition field c on Ω, solve the **equation of mechanical equilibrium**

$$\frac{\partial}{\partial r_j}\{C_{ijkl}(E_{kl} + \varepsilon^{\star}_{kl} - \varepsilon^0_{kl})\} = 0 \text{ on } \Omega, \tag{25}$$

with the **constraint**

$$E_{ij} = S_{ijkl}(\sigma^A_{kl} + \langle\{\sigma^0_{kl}\}\rangle - \langle\{\sigma^{\star}_{kl}\}\rangle) \tag{26}$$

and the **boundary condition**

$$\varepsilon^{\star}_{kl} \text{ is periodic on } \Omega. \tag{27}$$

Substituting for C_{ijkl}, and ε^0_{kl} in terms of composition, and $\varepsilon^\star_{kl}$ in terms of the displacement field in Eq. 25, and using the symmetry properties of the elastic constants and strains, we obtain

$$\frac{\partial}{\partial r_j}\left\{[C^{\rm eff}_{ijkl}+\alpha(c)\Delta C_{ijkl}]\left(E_{kl}+\frac{\partial u^\star_l(\mathbf{r})}{\partial r_k}-\varepsilon^T\delta_{kl}\beta(c)\right)\right\}=0. \tag{28}$$

$$\left[C^{\rm eff}_{ijkl}\frac{\partial^2}{\partial r_j\partial r_k}+\Delta C_{ijkl}\frac{\partial}{\partial r_j}\left(\alpha(c)\frac{\partial}{\partial r_k}\right)\right]u^\star_l(\mathbf{r})=C^{\rm eff}_{ijkl}\varepsilon^T\delta_{kl}\frac{\partial\beta(c)}{\partial r_j} -\Delta C_{ijkl}E_{kl}\frac{\partial\alpha(c)}{\partial r_j} +\Delta C_{ijkl}\varepsilon^T\delta_{kl}\frac{\partial\{\alpha(c)\beta(c)\}}{\partial r_j}. \tag{29}$$

In earlier work on the role of elastic inhomogeneity [33,19], the homogeneous strain E_{ij} was assumed to take a constant value. For example in Ref. [33], it is assumed to be zero, while in Ref. [19], where microstructural evolution is studied under an applied stress, a constant strain is imposed on the system through a constant E_{ij} tensor. In contrast, our present formulation allows for a prescribed overall stress (which is achieved by controlling the strain). This approach is known as "stress-control based on strain-control" (See Appendix D of [31]).

3.1 Computational algorithm

The equation of mechanical equilibrium, Eq. 29, can be solved numerically using an iterative procedure [38,33,31]. We begin with the zeroeth order approximation to the solution by assuming that $\Delta C_{ijkl}=0$. Thus, Eq. 15 reduces to:

$$C^{\rm eff}_{ijkl}\frac{\partial^2 u^\star_l(\mathbf{r})}{\partial r_j\partial r_k}=C^{\rm eff}_{ijkl}\varepsilon^T\delta_{kl}\frac{\partial\beta(c)}{\partial r_j}. \tag{30}$$

Taking $\sigma^T_{ij}=C^{\rm eff}_{ijkl}\varepsilon^T\delta_{kl}$,

$$C^{\rm eff}_{ijkl}\frac{\partial^2 u^\star_l(\mathbf{r})}{\partial r_j\partial r_k}=\sigma^T_{ij}\frac{\partial\beta(c)}{\partial r_j}. \tag{31}$$

The above equation can be solved in Fourier space. If we denote the Fourier transform of a quantity $(\cdot)$ by $\{(\cdot)\}_{\mathbf{g}}$,

$$\{(\cdot)\}_{\mathbf{g}} = \int_{\Omega} (\cdot) \exp\left(-2\pi J \mathbf{g}' \cdot \mathbf{r}\right) d\mathbf{r}, \tag{32}$$

where J is $\sqrt{(-1)}$. Defining G_{il}^{-1} as $C_{ijkl} g_j g_k$ (where $\mathbf{g} = 2\pi\mathbf{g}'$), we can write the solution (in the Fourier space) as follows:

$$\left\{(u_l^\star)^0\right\}_{\mathbf{g}} = -JG_{il}\sigma_{ij}^T g_j \{\beta(c)\}_{\mathbf{g}}, \tag{33}$$

where the superscript on $u_l^\star$ denotes the order of approximation.

Starting with the zeroth order approximation, it is now possible to refine the solution. We write the nth order refined solution using the $(n-1)$th order solution as follows:

$$\{(u_l^\star)^n\}_{\mathbf{g}} = -JG_{il}\Lambda_{ij}^{n-1} g_j, \tag{34}$$

where

$$\begin{aligned}\Lambda_{ij}^{n-1} = {} & \sigma_{ij}^T \{\beta(c)\}_{\mathbf{g}} - \Delta C_{ijmn} E_{mn}^{n-1} \{\alpha(c)\}_{\mathbf{g}} \\ & + \Delta C_{ijmn} \varepsilon^T \delta_{mn} \{\alpha[c(\mathbf{r})]\ \beta[c(\mathbf{r})]\}_{\mathbf{g}} - \Delta C_{ijmn} \left\{\alpha[c(\mathbf{r})] \frac{\partial (u_m^\star)^{n-1}(\mathbf{r})}{\partial r_n}\right\}_{\mathbf{g}},\end{aligned} \tag{35}$$

and, $\mathbf{E}^{n-1}$ is the homogeneous strain calculated from the $n-1$th order approximation of solution using Eq. 24.

3.2 Elastic contribution to chemical potential

The solution procedure yields periodic displacement $\mathbf{u}^\star$ and homogeneous strain $\mathbf{E}$, and hence strain field ε_{ij} (through Eq. 19 and 20), ε^{el} (through Eq. 9), and σ^{el} (through Eq. 11). Substituting for ε^{el} and σ^{el} in Eq. 8, and using the definition of μ^{el} in Eq. 4, we obtain

$$\begin{aligned}N_V \mu^{el} = {} & \frac{1}{2}\alpha'(c)\Delta C_{ijkl}(E_{ij} + \varepsilon_{ij}^\star - \varepsilon_{ij}^0)(E_{kl} + \varepsilon_{kl}^\star - \varepsilon_{kl}^0) \\ & -\beta'(c)\varepsilon^T \delta_{ij} C_{ijkl}(E_{kl} + \varepsilon_{kl}^\star - \varepsilon_{kl}^0),\end{aligned} \tag{36}$$

where the prime represents the differentiation with respect to c. Note that the above expression is the same as that given by equation 18 in [39].

3.3 Non-dimensionalisation

All the parameters used in our simulations are non-dimensional. We carry out the non-dimensionalisation using the characteristic length L', energy E', and time T' given below (where, the prime represents the fact that these quantities are dimensional):

$$L' = \left(\frac{\kappa'}{A'_b}\right)^{\frac{1}{2}}, \tag{37}$$

$$E' = A'_b, \tag{38}$$

$$T' = \frac{L'^2(c'_p - c'_m)^2}{M'E'}. \tag{39}$$

With these choices, we have $\kappa = 1$, $A_b = 1$, and $M = 1$. If $L' = 4\mathring{A}$, and $E' = 10^{-20}$ J, the choice of parameters given in Table 1, can be shown to yield an interfacial energy of 0.1 J m^{-2}, and a shear modulus of 300 GPa for the matrix phase.

3.4 Simulation algorithm

We start with the Fourier transform of Eq. 2:

$$\frac{\partial\{c\}_{\mathbf{g}}}{\partial t} = -g^2(\{h\}_{\mathbf{g}} + 2g^2\{c\}_{\mathbf{g}} + \{\mu^{el}\}_{\mathbf{g}}), \tag{40}$$

where $\mathbf{g}$ is a vector in the reciprocal space, $g = |\mathbf{g}|$ and $h(c) = \partial f_0/\partial c$ (see Eq. 7). The semi-implicit discretisation of this equation is [40]:

$$\frac{c(\mathbf{g}, t+\Delta t) - c(\mathbf{g}, t)}{\Delta t} = -g^2\{h\}_{\mathbf{g}} - 2g^4 c(\mathbf{g}, t+\Delta t) - g^2\{\mu^{el}\}_{\mathbf{g}}. \tag{41}$$

$$c(\mathbf{g}, t+\Delta t) = \frac{c(\mathbf{g}, t) - g^2\Delta t(\{h\}_{\mathbf{g}} + \{\mu^{el}\}_{\mathbf{g}})}{1 + 2\Delta t g^4}, \tag{42}$$

where Δt is the time step for the numerical integration. Thus the problem of microstructural evolution reduces to numerically solving the discretised equation(s) above.

Thus, for a given composition field at a given time, we solve the equation of mechanical equilibrium and obtain μ^{el} (using Eq. 36), and $h(c)$ (see Eq. 7),

and their Fourier transforms. They are used in Eq. 42 to compute the composition field at $t + \Delta t$, on which this process can be repeated to simulate microstructural evolution.

This simulation procedure requires solving the equation of mechanical equilibrium at each time step. For this, we need to (a) get the zeroth order solution (using Eq. 33), and (b) refine the zeroth order solution (using Eq. 34) to get higher order (and more accurate) solutions, until convergence is achieved. In this iterative method, it is possible, from the second time step onwards, to use the displacements from the previous time step as the starting point and thus expedite the iterative refinement. The solution is deemed to have converged if the error in displacements is less than a given value (typically, less than 10^{-8}). We use the L^2 norm in defining the error: Let $\mathbf{u}^n(i,j)$ and $\mathbf{u}^{n+1}(i,j)$ be the displacement solutions at the grid point (i,j). Let the total number of grid points in the x and y-directions be M and N respectively. Then, the error is

$$\text{Error} = \left[\sum_{i=1}^{M}\sum_{j=1}^{N}(\mathbf{u}^{n+1}(i,j) - \mathbf{u}^{n}(i,j)) \cdot (\mathbf{u}^{n+1}(i,j) - \mathbf{u}^{n}(i,j))\right]^{\frac{1}{2}}. \tag{43}$$

The (discrete) Fourier transforms needed for our calculations have been carried out using the free software FFTW (Fastest Fourier Transform in the West) developed by Frigo and Johnson [41].

4 Results I: Numerical Method

4.1 System parameters

All the parameters used in our computation are listed in Table 1. The cubic elastic constants are presented in terms of the average shear modulus G, the Poisson's ratio ν, and the anisotropy parameter A_Z, which are related [16] to the circular averages of the Voigt constants $\overline{C}_{11}$, $\overline{C}_{12}$, and $\overline{C}_{44}$:

$$G = \overline{C}_{44}, \tag{44}$$

$$\nu = \frac{1}{2}\frac{\overline{C}_{12}}{\overline{C}_{12} + \overline{C}_{44}}, \tag{45}$$

$$A_Z = \frac{2\overline{C}_{44}}{\overline{C}_{11} - \overline{C}_{12}}. \tag{46}$$

If A_Z, the anisotropy parameter is equal to unity, the elastic constants are isotropic. If it is greater (less) than unity, then the elastic constants have a cubic anisotropy, with $\langle 10 \rangle$ directions ($\langle 11 \rangle$ directions) being the softest [42,43]. We define an inhomogeneity ratio, δ, as the ratio of the shear modulus of the two phases p and m: $\delta = \overline{C}^p_{44}/\overline{C}^m_{44}$. If δ is equal to unity, then the system is elastically homogeneous. If it is greater (less) than unity, then the precipitate phase is harder (softer) than the matrix. In all our calculations, we use: $\nu^p = \nu^m = 0.3$, and $A^p_Z = A^m_Z$; thus elastic inhomogeneity enters our simulations only through δ.

Our choice for the interpolation function $\beta(c)$ for eigenstrain (see Eq. 12) is the same as that used by Wang et al [44]. This choice implies using the strain free matrix as the reference state, with respect to which all strains are measured. We use a similar function for $\alpha(c)$ that interpolates the elastic moduli of the two phases (see Eq. 13). This choice implies that our effective elastic modulus is the arithmetic mean of moduli of the two phases: $C^{\text{eff}}_{ijkl} = (C^m_{ijkl} + C^p_{ijkl})/2$.

4.2 Circular and elliptic precipitates

In Fig. 1, we compare the numerical solutions for the principal stress components (normalised by $G^m \varepsilon^T$) as a function of normalised distance (r/R) from the centre of a circular precipitate along the x-axis for an elastically isotropic system ($A_Z = 1$) with a softer precipitate $\delta = 0.5$. The corresponding analytical solutions [45,46] are also shown (using dotted lines) for a direct comparison. It is clear from Fig. 1 that the numerical and analytical solutions are in good agreement. In addition to reproducing the curve for σ_{11} (which is continuous at the particle-matrix interface), the numerical results are able to capture well the discontinuity in σ_{22} at the interface; further, σ_{12}, the shear stress, which must be identically zero everywhere, is less than 10^{-5} in our numerical calculations. Finally, the stress at the edge of the simulation cell is very nearly zero, indicating that our assumption of an effectively infinite matrix is indeed valid.

We have carried out similar comparisons of our numerical solutions for the strain components at the centre of elastically isotropic (circular and elliptic), soft ($\delta = 0.5$), homogeneous ($\delta = 1.0$), and hard ($\delta = 2.0$) precipitates, as well as for solutions inside a circular and an elliptic homogeneous precipitate when the elastic constants are anisotropic (with $A_Z = 3.0$) (with the corresponding analytical solutions given by Mura (p. 142 of [45]). In all the calculations, the error in the principal strain components (normalized by the misfit parameter ε^T) at the centre of the precipitate is 1.0% or less (for a volume fraction of ≈ 0.0075). Moreover, the shear strain components at the centre of the precipitates are identically zero for all these cases: in our numerical calculations

Parameter type	Parameter	Value used
Cahn-Hilliard Model	M	1.0
	κ	1.0
	A_b	1.0
Elastic	G^m/N_V	400.0
	ν	0.3
	ε^T	0.01 (for precipitates)
		0.0 (for cavities)
	α	$\{c^3(10-15c+6c^2)\}-\frac{1}{2}$
	β	$c^3(10-15c+6c^2)$
	C^{eff}_{ijkl}	$\frac{1}{2}(C^m_{ijkl}+C^p_{ijkl})$
Simulation	Δx	1.0
	Δy	1.0
	Δt	1.0
	Allowed error in displacements	less than 10^{-8}

Table 1
Parameters used in the simulations

also, we find that the unnormalised shear strain components are of the order of 10^{-5} or less.

4.3 Cavity under an externally applied stress

Stress fields around a cavity in a stressed material can also be studied by treating the cavity as a material with very small elastic moduli (i.e., $\delta \ll 1$). Our numerical solutions for a circular cavity in a plate under a uniaxial stress are shown in Fig. 2; we have used $\delta = 10^{-4}$. In this case too, we find a good agreement between our numerical results and the analytical solution (taken from page 91 of [47]).

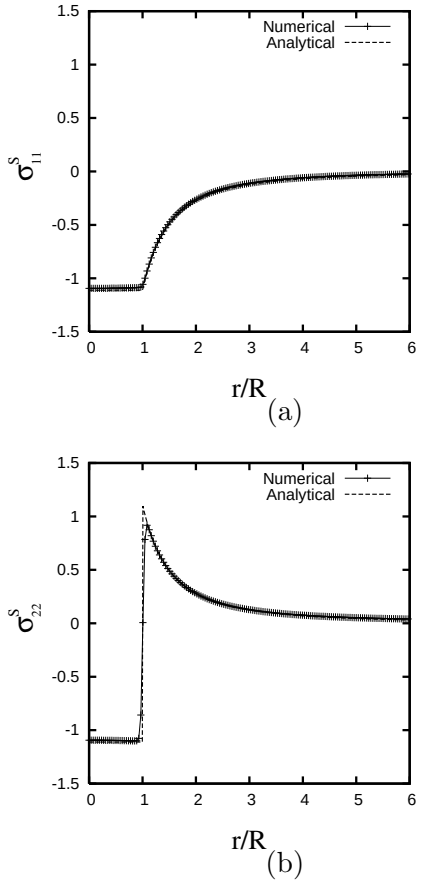

Fig. 1. The normalised stress components (a) σ^s_{11} and (b) σ^s_{22} as a function of normalised distance: analytical and numerical solutions along the x-axis (from the centre of a circular precipitate). The distance is normalised by R, the precipitate radius, while the stress is normalised by the characteristic stress $G^m\varepsilon^T$. The line through the data points is drawn only as a guide to the eye. $R = 25.8$; $L_x = L_y = 512$; $\delta = 0.5$; $A_Z = 1$.

4.4 Homogeneous strain

As a final benchmarking exercise, we plot in Fig. 3 (a) the (isotropic) homogeneous strain $\mathbf{E}$ normalised by ε^T as a function of volume fraction for homogeneous as well as inhomogeneous systems ($\delta = 0.5$ and $\delta = 2.0$) with a circular precipitate in the simulation box. Since the unstressed the matrix is the reference state for measuring strains, Khachaturyan showed that, for an elastically homogeneous system, the ratio E_{11}/ε^T must equal the volume fraction of the precipitate phase (see p.206 of [48]). Fig. 3 shows that this is indeed the case in our calculations. In the case of a hard (soft) precipitate in a soft (hard) matrix, the homogeneous strain is greater (smaller) than the volume fraction of the precipitate as expected. Further, as the volume fraction of the precipitate tends to zero, the homogeneous strain also tends to zero.

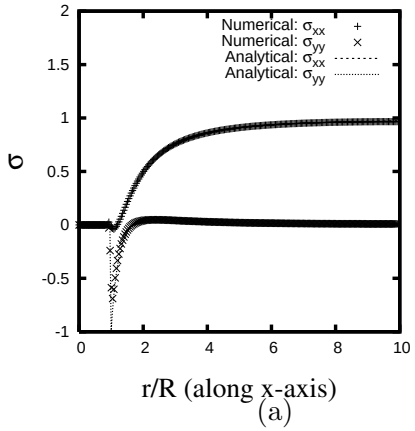

(a)

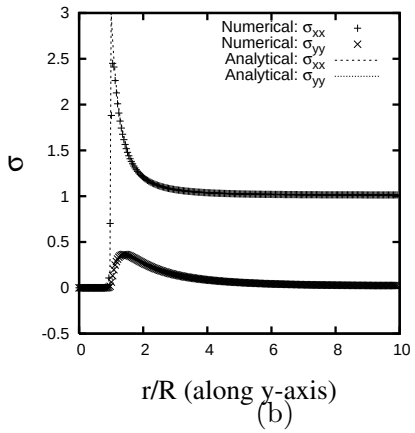

(b)

Fig. 2. The σ_{11} and σ_{22} stress components along the (a) x-axis and (b) y-axis from the centre of a circular cavity in a square domain under an applied tensile stress along the x-axis. $R = 25.8$; $L_x = L_y = 512$; $\sigma^A = 1$; $\delta = 10^{-8}$; $\varepsilon^T = 0$.

This exercise also allows us to estimate the error involved in using zero displacement condition (i.e., $\mathbf{E} = 0$) instead of zero traction condition ($\sigma_A = 0$) appropriate for an unstressed system. In Fig. 3 (b), we plot this (normalised) error in the elastic energy as a function of precipitate volume fraction. The normalisation was carried out using the elastic energy of the unstressed system ($\sigma^A = 0$). Even at a volume fraction of 0.2, the error could exceed 100%, and at a volume fraction of 0.5, it could be as large as 500%.

How significant is this error in simulations of microstructural evolution? We have compared [34] microstructural evolution under two different boundary conditions: $\mathbf{E} = 0$ and $\sigma_A = 0$. Since the former overestimates the elastic energy, we found that its microstructural evolution is equivalent to that of the latter with a higher modulus (or, equivalently, higher eigenstrain).

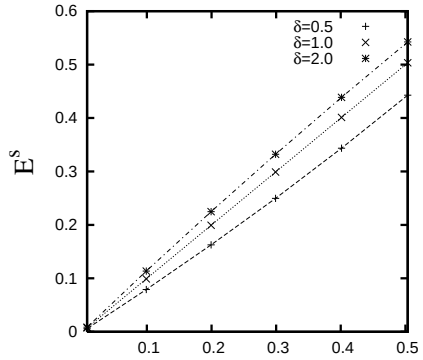

(a)

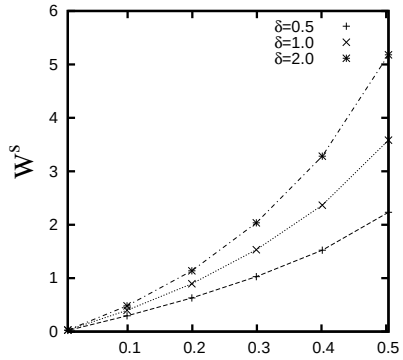

(b)

Fig. 3. The (a) normalised homogeneous strain and (b) the normalised difference in the elastic energy as a function of the volume fraction of the precipitate. The homogeneous strain is normalised by the strength of the eigenstrain $\varepsilon^T = 0.01$, while, the elastic energy was normalised by the elastic energy for an unconstrained system. The lines through the data points are drawn only as a guide to the eye.

5 Results II. Rafting

5.1 Single particle rafting

Before we present our results on rafting in multiparticle systems, we first summarize the salient results for single particle. Among the numerous thermodynamic (or, energy-based) attempts in the literature to determine the type of rafting due to elastic stresses [12–16] (see the review Chang and Allen [10], the analysis of Schmidt and Gross [16] (hereafter, referred to as SG) is the most general and complete. Assuming the particle shapes to conform to cubic (four-fold) symmetry, SG predicted the direction of elongation in systems with elastic isotropy and cubic anisotropy (in 2D as well as 3D).

The 2D results of SG are summarised schematically in the Fig. 4. The applied

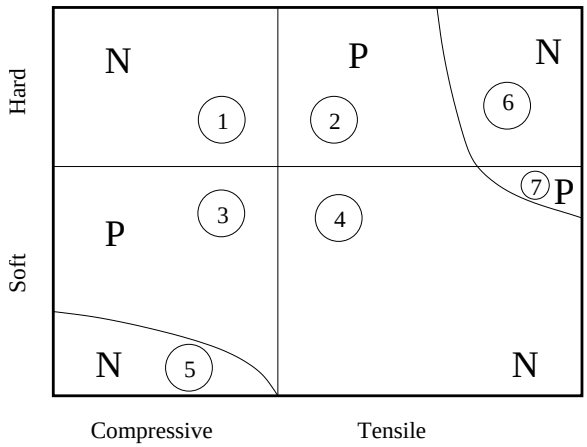

Fig. 4. Schematic rafting behaviour based on the analysis of Schmidt and Gross (Ref. [16], Fig. 3), assuming a positive dilatational eigenstrain and an applied stress along the x-axis on particles with four-fold symmetry.

stress is along the x-axis, and the eigenstrain is assumed to be positive. The regions 1 and 3 correspond to hard particle under compressive stress and soft particle under tensile stress respectively; hence, it leads to N-type rafting; in a similar manner, regions 2 and 4 which correspond to hard particle under tensile stress and soft particle under tensile stress respectively, leading to a P-type rafting. While the SG results have been criticized in Ref. [49], we wish to point out that our own simulations of evolution of a single particle [34] confirm the SG results on the direction of elongation.

Further, in addition to regions 1 to 4 in Fig. 4, SG also report the existence of several other regions appear towards outer extremities. Region 5, for example, corresponds to a very compliant precipitate under compressive stress; we have been able to confirm this region as well [34].

Regions 6 and 7, on the other hand, appear only in those systems in which the two constituent phases have different Poisson's ratio and/or Zener anisotropy parameter. Since we assume $\nu^p = \nu^m$ and $A_Z^p = A_Z^m$ in our calculations, our simulations cannot validate this result.

5.1.1 Simulations of multiparticle rafting

The initial microstructure in these simulations is prepared by randomly placing 900 particles of radius $R = 5$ in the simulation box. The supersaturation in the matrix is such that the overall alloy composition (equilibrium volume fraction) is 0.4. The precipitates have a positive dilatational misfit ($\varepsilon^T = 0.01$) with respect to the matrix phase. All the results presented here are for systems that fall under the first four categories of Schmidt and Gross in Fig. 4.

First, we note that in all the rafting simulations, the direction of elongation

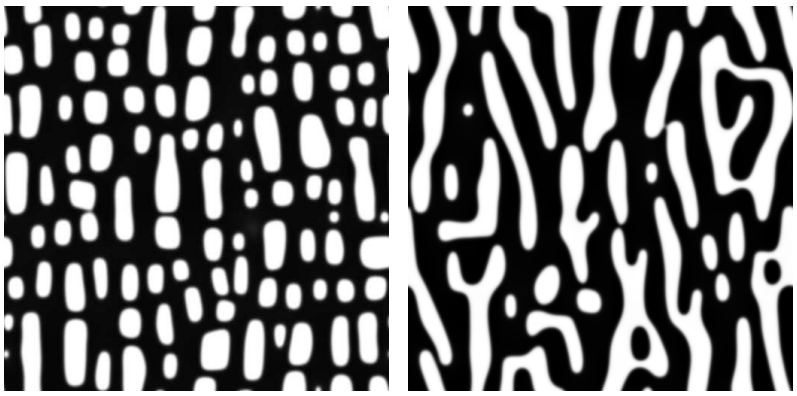

(a) (b)

Fig. 5. Rafting in an anisotropic system of (a) hard particles ($\delta = 2$) under a tensile stress along the y-axis and (b) soft particles ($\delta = 0.5$) under a tensile stress along the x-axis; microstructures after 3000 time units. $A_Z = 3$; $|\sigma^A| = 0.01G^m$; $c_0 = 0.4$.

observed in the microstructures is consistent with theoretical predictions [16]. However, in order to enable easier comparison, we present our results in such a way that particle elongation is along the y-axis in all the figures; this is achieved by choosing the stress direction appropriately.

Fig. 5 shows the typical microstructural evolution in an anisotropic system ($A_Z = 3$) with (a) hard precipitates under tensile stress along the y-axis, and (b) soft precipitates under tensile stress along the x-axis. Note that in both cases the applied stress is tensile. In this figure, it is clear that hard particles are smaller and less elongated than soft particles. In other words, hard precipitates are better than soft ones in resisting rafting and retaining their compact shapes.

A uniaxial applied stress produces directional (i.e., elongated and aligned) microstructures not only in elastically anisotropic systems, but also in isotropic ones, as can be seen in Fig. 6, which is for an isotropic system with soft precipitates. The upper figure is for a tensile stress along x-axis, and the lower one is for a compressive stress along y-axis. Thus, both cases, the particles elongate along the y direction.

This figure also shows the effect of the sign of the applied stress on rafted morphologies. While the direction of elongation is the same in both figures, the morphologies in the two cases are different. The precipitates are smaller and less elongated in the system under a compressive stress (b). Thus, rafting is more pronounced when σ^A and ε^T have the same sign, than when they have opposite signs.

In Figs. 6, and 5, the soft particles also appear to have undergone significant coalescence, leading to particle morphologies that are wiggly and imperfectly aligned. In Fig. 5, the elastic anisotropy ($A_Z = 3$) is such that particles would

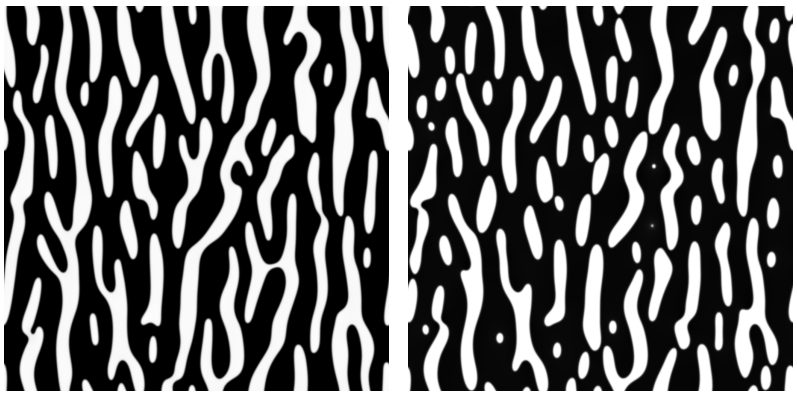

(a) (b)

Fig. 6. Soft particles in an isotropic system under (a) a tensile stress along the x-axis and (b) a compressive stress along the y-axis; microstructures after 9000 time units. $A_Z = 1$; $\delta = 0.5$; $|\sigma^A| = 0.01 G^m$; $c_0 \approx 0.35$.

align along the x and y axes ($\langle 10 \rangle$ directions) even without an applied stress. When a stress is applied along one of these directions, the alignment along the rafting direction is far stronger than that along the non-rafting direction. In Fig. 5 a, for example, particles do exhibit a strong alignment along the y-axis (rafting direction); still some alignment along the x-axis can also be discerned.

The role of anisotropy can be seen more clearly in systems with $A_Z < 1$, in which the $\langle 11 \rangle$ directions are preferred for alignment in the absence of an applied stress. In Fig. 7 we show the microstructures systems with $A_Z = 1/3$. While they exhibit a strong alignment along the $\langle 11 \rangle$ directions (top row) in the absence of an applied stress, the alignment of the particles does shift towards the rafting directions when a stress is applied. For example, in Fig. 7, the evolution of soft precipitates under an applied tensile stress along the x-axis should lead to rafting along the y-axis (N type rafting); this figure does show rafting along a direction intermediate between the y-axis and $\langle 11 \rangle$ directions.

6 Discussion

6.1 Numerical solution of the equation of mechanical equilibrium

For linear elastic constitutive laws (as well as perfect plasticity and linear visco-elasticity), the homogenisation problem is known to be well-posed [30]. Further, Hu and Chen [33] also show that each iteration in an iterative procedure of the type described above corresponds to a given order of approximation of the Green function expansion in the formulation of Khachaturyan et al [38].

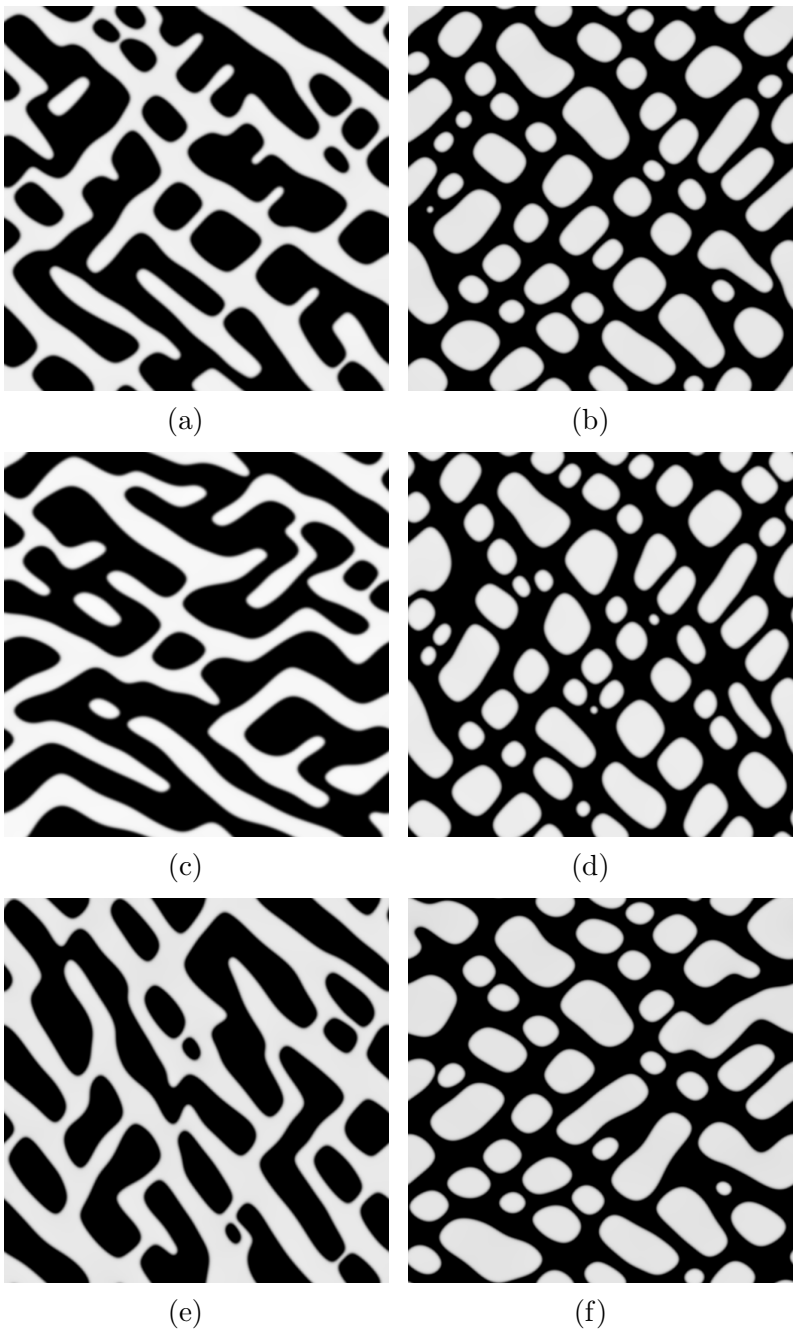

Fig. 7. Microstructures in (a) Soft, (b) Hard, (c) Soft-Compressive, (d) Hard-Compressive, (e) Soft-Tensile, and (f) Hard-Tensile systems after 8000 time units in an elastically anisotropic system. The applied stresses are along the x-axis. $A_Z = 1/3$; $\delta = 2$ (hard); $\delta = 0.5$ (soft); $|\sigma^A| = 0.005G^m$; $c_0 = 0.4$.

Thus, our iterative procedure, outlined in this paper is expected to converge.

However, we wish to highlight two interesting practical observations about the convergence of our iterative algorithm. First, an iterative procedure based on FFT for homogenisation studies is known to converge slowly as the 'contrast'

($\delta \ll 1$) widens [31]; i.e., as δ approaches zero (cavities are modeled using vanishingly small but finite δ values). But, as shown in Fig. 8, we get, in practice, an (encouragingly) fast convergence even for cavities ($\delta \ll 1$) using the above methodology within 23 iterations, when cavity volume fraction is less than 1 %; however, for a volume fraction of 30%, and $\delta = 10^{-6}$, this number is larger (~ 99).

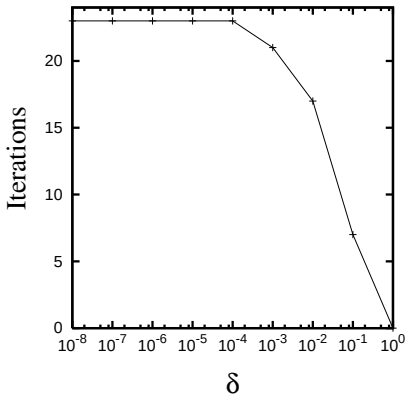

Fig. 8. The effect of inhomogeneity on convergence; data from simulations of a circular cavity in a square domain under an externally applied uniaxial stress (Fig. 2). The line through the data points is drawn only as a guide to the eye.

A second interesting result from our calculations is presented in Table 2. In the iterative procedure for solving for mechanical equilibrium, the definition used for C^{eff}, the "effective moduli" (with which we calculate the zeroth order solution, Eqn. 33) has a strong effect on convergence. In Table 2, we list the number of iterations needed to converge to the solution in three different cases, viz., $\frac{1}{2}(C^m + C^p)$, C^m and C^p. Even though all the three expressions lead to the same solution, using C^m or C^p as the effective modulus increases the number of iterations by one or two orders of magnitude compared to the case when $C^{\text{eff}} = \frac{1}{2}(C^m + C^p)$. Surprisingly, when we use the arithmetic average, the number of iterations needed for convergence is roughly independent of whether the precipitate is harder or softer than the matrix; at present, the reason for this faster convergence is not clear.

6.2 Rafting in multiparticle systems

Our multiparticle simulations (Figs. 6, and 5), show that the direction of elongation are in agreement with the results from thermodynamic models [16]; they are also in agreement with the kinetic studies based on atomistic models [21–24] and continuum models [17–20].

The morphological changes in multiparticle simulations have a significant contribution from elastic interactions among particles. In particular, such inter-

Inhomogeneity	Expression for C^{eff}_{ijkl}	Number of iterations
Hard precipitate ($\delta = 2.0$)	$\frac{1}{2}(C^p_{ijkl} + C^m_{ijkl})$	4
	C^m_{ijkl}	93
	C^p_{ijkl}	5
Soft precipitate ($\delta = 0.5$)	$\frac{1}{2}(C^p_{ijkl} + C^m_{ijkl})$	4
	C^m_{ijkl}	7
	C^p_{ijkl}	620

Table 2
The effect of interpolation function α and the corresponding C^{eff}_{ijkl} on convergence.

actions lead to particle migration (in hard precipitates), and coalescence and migration (in soft precipitates).

The particle coalescence and migration can be more clearly discerned using two-particle simulations (see Fig. 9). The initial configuration has two particles of radius $R = 10$ placed at a distance of about $3R$ in a 512×512 simulation cell such that the line joining their centres of mass makes an angle of 45° with the x-axis. The far-field composition is maintained at 0.1.

The microstructures (after 5000 time units) corresponding to regions 1, 2, 3, and 4 of the schematic in Fig. 4 are shown in the Fig. 9 a, b, c, and d, respectively In all cases the particles try to align along the x- or y-axes; this direction is consistent with the direction of elongation predicted for single particle geometries. However, while the hard particles migrate, the soft particles both migrate and coalesce. The migration of the hard particles is clear from Fig. 9 (e), where the angle θ that the line joining the centres of mass of the two hard particles makes with the x-axis keeps shifting in the expected direction with time.

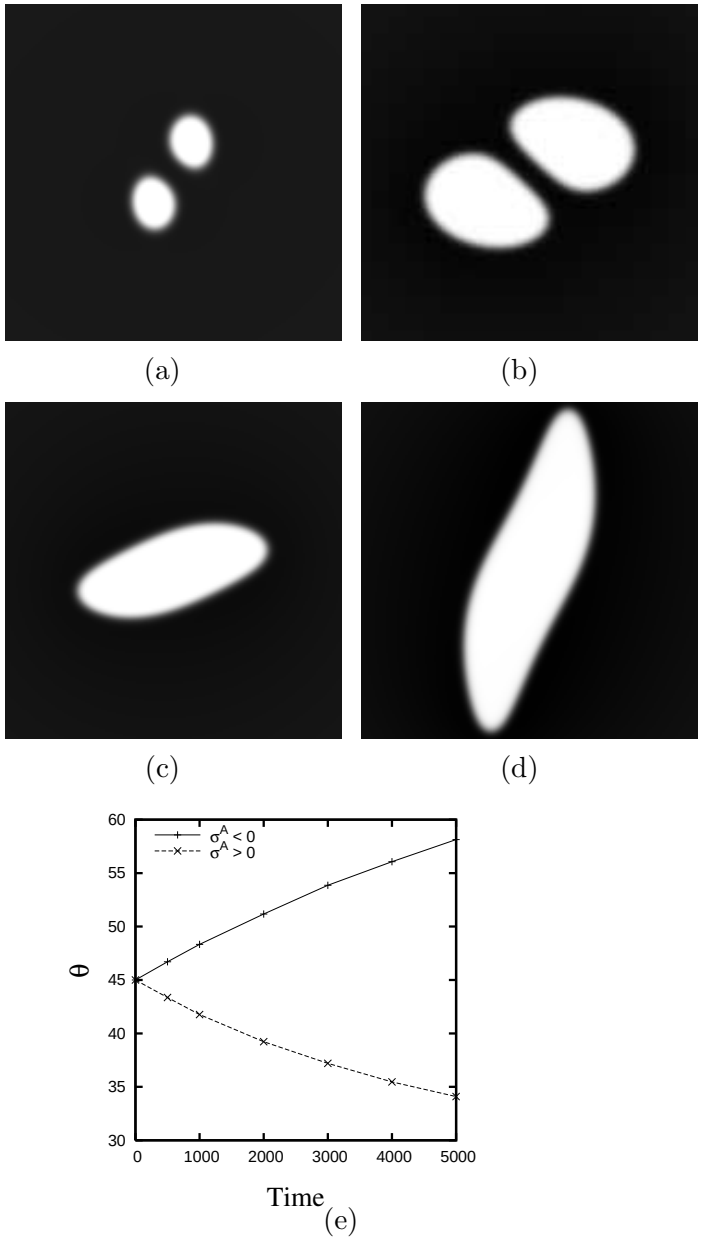

Fig. 9. (a) Hard particles under compressive stress (b) Hard particles under tensile stress (c) Soft particles under compressive stress (d) Soft particles under tensile stress. Applied stresses are along the x-axis. All the microstructures correspond to 5000 time units. Note that (a), (b), (c), and (d) correspond to regions (1), (2), (3), and (4) of the schematic 4 respectively. $A_Z = 1$; $\delta = 2$ (hard); $\delta = 0.5$ (soft); $|\sigma^A| = 0.01 G^m$; $c_0 = 0.1$. (e) The angle θ that the line joining the centres of mass of two hard particles makes with the x-axis as a function of time.

7 Conclusions

(1) We present a phase field model which incorporates an iterative algorithm for numerically solving the equation of mechanical equilibrium in an elastically inhomogeneous system.

(2) The iterative method used for solving the equation of mechanical equilibrium is capable of handling both prescribed traction and displacement boundary conditions (and is the same as the stress-control-via-strain-control approach used in the homogenisation literature).
(3) Using our phase field model, we show that purely elastic stress driven rafting is possible, and, that the rafting type in such systems is predicted correctly by thermodynamic studies of Schmidt and Gross [16].
(4) Rafting is more pronounced when precipitates are softer and the sign of the applied stress is the same as that of the misfit.
(5) In the case of multiparticle rafting, interparticle interactions leading to particle migration has a significant contribution to the rafted microstructure. Further, in the case of soft precipitates, particle coalescence also contributes to preferential coarsening.

8 Acknowledgements

We thank Professors F. Haider, C.S. Jog, and Vijay Shenoy for many helpful discussions and the Volkswagen Foundation for financial assistance.

References

[1] W. C. Johnson, Influence of elastic stress on phase transformations, in: H. I. Aaronson (Ed.), Lectures on the theory of phase transformations, Second Edition, TMS, 184, Thorn Hill Road, Warrendale, Pennsylvania 15086-7528, 1999, pp. 35–134.

[2] M. Doi, Elasticity effects on the microstructure of alloys containing coherent precipitates, Progress in Materials Science 40 (1996) 79–180.

[3] P. Fratzl, O. Penrose, J. L. Lebowitz, Modeling of phase separation in alloys with coherent elastic misfit, Journal of Statistical Physics 95 (5/6) (1999) 1429–1503.

[4] P. W. Voorhees, W. C. Johnson, The thermodynamics of elastically stressed crystals, Vol. 59 of Solid state physics: advances in research and applications, Elsevier academic press, 2004, pp. 1–201.

[5] J. K. Tien, S. M. Copley, The effect of uniaxial stress on the periodic morphology of coherent gamma prime precipitates in nickel-base superalloy crystals, Metallurgical Transactions 2 (1971) 215–219.

[6] A. Onuki, H. Nishimori, Anomalously slow domain growth due to a modulus inhomogeneity in phase-separating alloys, Physical Review B 43 (16) (1991) 13649–13652.

[7] N. Sridhar, J. M. Rickman, D. J. Srolovitz, Microstructural stability of stressed lamellar and fiber composites, Acta Materialia 45 (7) (1997) 2715–2733.

[8] M. P. Gururajan, T. A. Abinandanan, A phase field study of microstructural evolution in elastically inhomogeneous systems, in: J. M. Howe, D. E. Laughlin, J. K. Lee, U. Dahmen, W. A. Soffa (Eds.), Proceedings of solid-solid phase transformations in inorganic materials 2005, May 29th – June 3rd, 2005, Vol. 2, TMS, 2005, p. 747.

[9] F. Louchet, M. Véron, Y. Bréchet, A. Hazotte, J. Y. Buffière, P. Bastie, A. Royer, New trends in directional coarsening of superalloys under stress, La revue de Métallurgie-CIT/Science et Génie des Matériaux (1998) 1481–1490.

[10] J. C. Chang, S. M. Allen, Elastic energy changes accompanying gamma-prime rafting in nickel-base superalloys, Journal of Materials Research 6 (9) (1991) 1843–1855.

[11] M. Kamaraj, Rafting in single crystal nickel-base superalloys – an overview, Sādhanā 28 (1/2) (2003) 115–128.

[12] F. R. N. Nabarro, C. M. Cress, P. Kotschy, The thermodynamic driving force for rafting in superalloys, Acta Materialia 44 (8) (1996) 3189–3198.

[13] A. Pineau, Influence of uniaxial stress on the morphology of coherent precipitates during coarsening – elastic energy considerations, Acta Metallurgica 24 (1976) 559–564.

[14] W. C. Johnson, Precipitate shape evolution under applied stress - thermodynamics and kinetics, Metallurgical Transactions A 18A (1987) 233–247.

[15] W. C. Johnson, M. B. Berkenpas, D. E. Laughlin, Precipitate shape transitions during coarsening under uniaxial stress, Acta Metallurgica 36 (12) (1988) 3149–3162.

[16] I. Schmidt, D. Gross, Directional coarsening in Ni-base superalloys: analytical results for an elasticity based model, Proceedings of Royal Society (London) A 455 (1999) 3085–3106.

[17] D. Y. Li, L. Q. Chen, Computer simulation of morphological evolution and rafting of γ' particles in Ni-base superalloys under applied stresses, Scripta Materialia 37 (9) (1997) 1271–1277.

[18] D. Y. Li, L. Q. Chen, Shape evolution and splitting of coherent particles under applied stresses, Acta Materialia 47 (1) (1999) 247–257.

[19] J. Zhu, L.-Q. Chen, J. Shen, Morphological evolution during phase separation and coarsening with strong inhomogeneous elasticity, Modelling and Simulation in Materials Science and Engineering 9 (2001) 499–511.

[20] P. H. Leo, J. S. Lowengrub, Q. Nie, On an elastically induced splitting instability, Acta Materialia 49 (2001) 2761–2772.

[21] J. K. Lee, Effects of applied stress on coherent precipitates via a discrete atom method, Metals and Materials 2 (3) (1996) 183–193.

[22] J. K. Lee, Studying stress-induced morphological evolution with the Discrete Atom Method, Journal of Metals 49 (12) (1997) 37–40,58.

[23] C. A. Laberge, P. Fratzl, J. L. Lebowitz, Microscopic model for directional coarsening of precipitates in alloys under external load, Acta Materialia 45 (10) (1997) 3949–3961.

[24] H. Gupta, R. Weinkamer, P. Fratzl, J. L. Lebowitz, Microscopic computer simulations of directional coarsening in face-centered cubic alloys, Acta Materialia 49 (2001) 53–63.

[25] T. M. Pollock, A. S. Argon, The role of creep deformation in directional coarsening of γ' in nickel-base single crystals, in: C. Pande, S. Marsh (Eds.), Modelling of coarsening and grain growth, The Minerals, Metals & Materials Society, 1993, pp. 35–44.

[26] T. M. Pollock, A. S. Argon, Directional coarsening in nickel-base single crystals with high volume fractions of coherent precipitates, Acta Metallurgica et Materialia 42 (6) (1994) 1859–1874.

[27] M. Véron, Y. Bréchet, F. Louchet, Strain induced directional coarsening in Ni based alloys, Scripta Materialia 34 (12) (1996) 1883–1886.

[28] M. Véron, P. Bastie, Strain induced directional coarsening in nickel based superalloys: investigation on kinetics using the small angle neutron scattering (sans) technique, Acta Materialia 45 (8) (1997) 3277–3282.

[29] O. Paris, M. Fährmann, E. Fährmann, T. M. Pollock, P. Fratzl, Early stages of precipitate rafting in a single crystal Ni-Al-Mo model alloy investigated by small-angle X-ray scattering and TEM, Acta Materialia 45 (3) (1997) 1085–1097.

[30] A. Anthoine, Derivation of the in-plane elastic characteristics of masonry through homogenization theory, International Journal of Solids and Structures 32 (2) (1995) 137–163.

[31] J. C. Michel, H. Moulinec, P. Suquet, Effective properties of composite materials with periodic microstructure: a computational approach, Computer Methods in Applied Mechanics and Engineering 172 (1999) 109–143.

[32] H. Moulinec, P. Suquet, A numerical method for computing the overall response of nonlinear composites with complex microstructure, Computer Methods in Applied Mechanics and Engineering 157 (1998) 69–94.

[33] S. Y. Hu, L. Q. Chen, A phase-field model for evolving microstructures with strong elastic inhomogeneity, Acta Materialia 49 (2001) 1879–1890.

[34] M. P. Gururajan, Elastic inhomogeneity effects on microstructures: a phase field study, Ph.D. thesis, Department of Metallurgy Indian Institute of Science Bangalore India 560012 INDIA, (The relevant chapters of this thesis are available for download at http://imechanica.org/node/440 as a pdf file.) (2006).

[35] J. W. Cahn, On spinodal decomposition, Acta Metallurgica 9 (1961) 795–801.

[36] L.-Q. Chen, Phase-field models for microstructure evolution, Annual Reviews of Materials Research 32 (2002) 113–140.

[37] Y. M. Jin, Y. U. Wang, A. G. Khachaturyan, Three-dimensional phase field microelasticity theory and modeling of multiple cracks and voids, Applied Physics Letters 79 (19) (2001) 3071–3073.

[38] A. G. Khachaturyan, S. Semenovskaya, T. Tsakalakos, Elastic strain energy of inhomogeneous solids, Physical Review B 52 (22) (1995) 15909–15919.

[39] P. H. Leo, J. S. Lowengrub, H. J. Jou, A diffuse interface model for microstructural evolution in elastically stressed solids, Acta Materialia 46 (6) (1998) 2113–2130.

[40] L. Q. Chen, J. Shen, Applications of semi-implicit Fourier-spectral method to phase field equations, Computer Physics Communications 108 (1998) 147–158.

[41] M. Frigo, S. G. Johnson, The design and implementation of FFTW3, Proceedings of the IEEE 93 (2) (2005) 216–231, special issue on "Program Generation, Optimization, and Platform Adaptation"; also see `http://www.fftw.org/`.

[42] R. Sankarasubramanian, C. S. Jog, T. A. Abinandanan, Symmetry-breaking transitions in equilibrium shapes of coherent precipitates: effect of elastic anisotropy and inhomogeneity, Metallurgical and Materials Transactions A 33A (2002) 1083–1090.

[43] J. F. Nye, Physical properties of crystals, 1st Edition, Oxford at the Clarendon Press, 1957.

[44] S. J. Wang, R. F. Sekerka, A. A. Wheeler, B. T. Murray, S. R. Coriell, R. J. Braun, G. B. McFadden, Thermodynamically-consistent phase-field models for solidification, Physica D 69 (1993) 189–200.

[45] T. Mura, Micromechanics of defects in solids, 1982nd Edition, Kluwer academic publishers, 1998 (Reprint, incorporating minor corrections in 1991).

[46] M. A. Jaswon, R. D. Bhargava, Two-dimensional elastic inclusion problems, Proceedings of Cambridge Philosophical Society 57 (1961) 669–680.

[47] S. P. Timoshenko, J. N. Goodier, Theory of elasticity, 3rd Edition, Mc-Graw Hill, 1970.

[48] A. G. Khachaturyan, Theory of structural transformations in solids, Wiley-Interscience Edition, John Wiley & Sons, 1983.

[49] T. Ichitsubo, D. Koumoto, M. Hirao, K. Tanaka, M. Osawa, T. Yokokawa, H. Harada, Rafting mechanism for Ni-base superalloy under external stress: elastic or elastic-plastic phenomena?, Acta Materialia 51 (14) (2003) 4033–4044.